Colloids and Surfaces A: Physicochemical and Engineering Aspects 672 (2023) 131697

Contents lists available at ScienceDirect

Colloids and Surfaces A: Physicochemical and Engineering Aspects

journal homepage: www.elsevier.com/locate/colsurfa

Low-cost, ecofriendly, and large-scale synthesis of nanostructured $Co_{1-x}Mn_xFe_2O_4$ microgranules with enhanced magnetic performance by chemical spray drying processing

Sumayya M. Ansari [a,b,g], Debasis Sen [c,d,g], Keerthi Haritha [e,g], Yesh D. Kolekar [a,g,*], C.V. Ramana [e,f,g,**]

[a] Department of Physics, Savitribai Phule Pune University, Pune 411007, India
[b] Department of Physics, United Arab Emirates University, P.O. Box 15551, Al Ain, United Arab Emirates
[c] Solid State Physics Division, Bhabha Atomic Research Centre, Mumbai 400 085, India
[d] Homi Bhabha National Institute, Anushaktinagar, Mumbai 400094, India
[e] Department of Aerospace and Mechanical Engineering, University of Texas at El Paso, 500 W. Univ. Ave., El Paso, TX 79968, USA
[f] Center for Advanced Materials Research (CMR), University of Texas at El Paso, 500 W. Univ. Ave., El Paso, TX 79968, USA
[g] Department of Aerospace & Mechanical Engineering, University of Texas at El Paso, 500 W. Univ. Ave., El Paso, TX 79968, USA

GRAPHICAL ABSTRACT

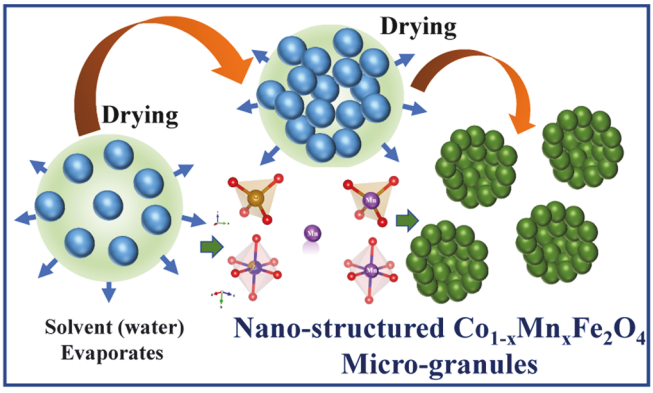

ARTICLE INFO

Keywords:
Cobalt ferrite
Ecofriendly synthesis
Large-scale manufacturing
Magnetic performance

ABSTRACT

We report, for the first time, the low-cost, eco-friendly, and large-scale synthesis of spray-drying production of Mn-substituted $CoFe_2O_4$ ($Co_{1-x}Mn_xFe_2O_4$; $x = 0.0–0.2$; CMF) microgranules and their structural, morphological, and magnetic properties and performance characteristics in detail. The comprehensive study explored the intimate relationships between cation disorder or inversion degree due to Mn substitution in $CoFe_2O_4$ (CF) microgranules and corresponding changes in the structural and magnetic properties. Crystal structure and morphology studies indicate the formation of spherical shape, single cubic mixed inverse spinel structure of all the CMFO-

* Corresponding author at: Department of Physics, Savitribai Phule Pune University, Pune 411007, India.
** Corresponding author at: Department of Aerospace and Mechanical Engineering, University of Texas at El Paso, 500 W. Univ. Ave., El Paso, TX 79968, USA
E-mail addresses: ydkolekar@gmail.com (Y.D. Kolekar), rvchintalapalle@utep.edu (C.V. Ramana).

https://doi.org/10.1016/j.colsurfa.2023.131697
Received 10 March 2023; Received in revised form 16 May 2023; Accepted 20 May 2023
Available online 22 May 2023

microgranules with a size variation in the range of ~6.5–7.5 μm. Small angle X-ray scattering analyses indicate that the nanostructured CMF microgranules exhibit a virtually hard-sphere-like interaction. It is concluded that distortions are related to Co ions at octahedral locations due to Mn substitution in all materials. Raman spectroscopic studies, which corroborate with other structural studies, also reveal that replacing Co with Mn increases the degree of inversion in the cubic inverse spinel structure. Divalent (Co^{2+}, Mn^{2+}) and trivalent (Fe^{3+}, Mn^{3+}) cations are distributed differently across tetrahedral and octahedral sites. In addition to large-scale chemical synthesis, our results demonstrate the enhanced magnetic saturation from 82.27 to 86.18 emu/gm and 77.05–79.87 emu/gm for $Co_{0.9}Mn_{0.1}Fe_2O_4$ at 10 K and 300 K, respectively. In order for the proposed architectural design to serve as a crucial building block for a wide range of technological applications and be applicable to a large class of spinel ferrites, we present our attempt to draw the necessary fundamental scientific explanation from the trends in the local structural parameters and magnetic characteristics of CMF nanomaterials.

1. Introduction

Nanoscale spinel ferrite particles have exceptional magnetic, electrical, and optical capabilities [1–3], making them a desirable building blocks for creating new technologies [4–12]. In addition, the nano-ferrite family has proved essential in promoting innovation across a wide range of disciplines, most notably biomedicine [1], catalysis [2], environmental remediation [13], and microwave technologies [14]. Cobalt ferrite ($CoFe_2O_4$; CF) has been studied extensively as an alternative to magnetite (Fe_3O_4) among the spinel-type ferrite systems owing to its superior chemical resistance to oxidation and inherent magnetic characteristics[15]. Because of its high coercivity and magnetocrystalline anisotropy [16], $CoFe_2O_4$ is the material of choice for high-density information storage and stress-sensing applications. The thermal stability of cobalt ferrite is well established up to 1000 °C. $CoFe_2O_4$ is a promising material for splitting methane into hydrogen because of its solid thermal stability [17]. Because of its superior magnetic anisotropy compared to other nano-ferrites [18], it is attracting increasing interest in biological applications. The ability to modify the structural and magnetic configuration of the $CoFeO_4$ ferrite by switching the identities of the Co^{2+} and Fe^{3+} cations is a crucial characteristic that has revolutionized applied technology and basic research. It has been suggested that the electrical, magnetic, and magneto-mechanical characteristics of CF may be modified by replacing cations for Fe[19–22]. On the other hand, the research and development of many researchers focused to designing new compositions with Co substitution in CF, namely with (nickel (Ni^{2+})[23], zinc (Zn^{2+})[24], palladium (Pd^{2+})[25], magnesium (Mg^{2+}) [26], copper(Cu^{2+}) [27], aluminum(Al^{2+}) [28], calcium(Ca^{2+})) [29]. However, among the many proposed cation substitutions, Mn substitution within CF attracted the scientific and engineering community because of the saturation magnetization enhancement compared to others [30–33]. Diverse strategies, such as the low-temperature chemical method, hydrothermal [30], sol-gel [34], co-precipitation [15], auto combustion [33], the polyol method [35], and ceramics method [36], have been adopted to synthesize nano and bulk form of $Co_xMn_{1-x}Fe_2O_4$ (CMF) mixed ferrites. Most of these methods, however, were either time-consuming or complicated (requiring high temperatures, organic solvents, and post-synthesis processing) or resulted in ferrite products with large particle sizes, irregular shapes, and agglomerated with low yield. In this context, herein, we directed our efforts to low-cost, eco--friendly, fast-processing, and large-scale synthesis of magnetic ferrites using chemical approach.

Sustainable, less time-consuming, and repeatable technologies for large-scale synthesis are currently being sought in this topical area of nanostructured materials for magnetic, electromagnetic, electronic and optoelectronic applications. However, it is still a significant challenge for scientists and engineers to develop nano- and bulk-scale magnetic ferrites with structural, magnetic, and electrical characteristics tailored to specific uses. Specifically, the precise control of the phase, structure and morphology, surface area, and size and/or size-distribution during the chemical reaction is a challenging, even if those synthetic procedures enable materials' production with a narrow size distribution. Furthermore, since many cutting-edge technological applications are sensitive not only to nano-size features of the crystals but also to a material with uniformity in crystal size, large-scale production of uniformly sized magnetic nanoparticles is essential. Studies have revealed, for instance, that size/size distribution has a significant role in determining the mechanical and thermal stability of magnetic nanofluids employed as heat transfer medium. Most importantly, note that public safety will be under jeopardy because of natural disasters and climate anomalies brought on by rising global carbon emissions. Therefore, there is an increasing global awareness on carbon neutrality in an effort to mitigate the environmental pollution crisis. Low-carbon technology is also essential toward realizing these emerging synthetic routes, technologies while improving public health at any cost. On the other hand, building ordered microscale or nanoscale structures without affecting the ecosystems is quite important in an extensive range of fields, such as biomedicines, targeting drugs, microsensors, heat transfer devices and advanced functional materials [37–41]. In this context, we present the spray-drying manufacturing of magnetic $CoFe_2O_4$ and Mn-substituted $CoFe_2O_4$ microgranules synthesized from an aqueous solution of the precursor elements (Fig. 1a). Our approach to synthesize CF and CFM in a large scale is presented in Fig. 1, where the key idea of Mn occupying

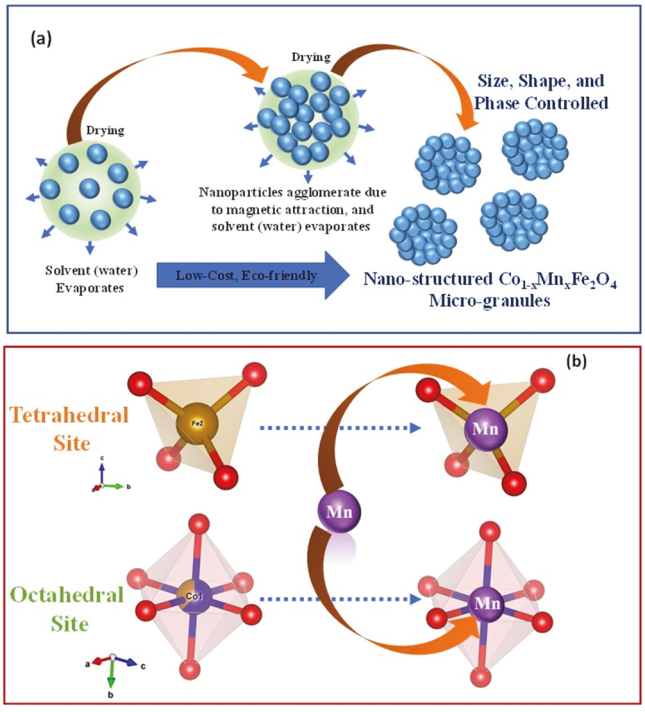

Fig. 1. (a) Schematic representation of the formation mechanism of nanostructured $Co_{1-x}Mn_xFe_2O_4$ micro-granules during spray drying; (b) The key approach of Mn into CF spinel crystal structure in terms of specific site occupation is shown.

the specific sites in CF is also illustrated (Fig. 1b). Spray drying is more environmentally friendly than other methods since it uses inexpensive chemicals and aqueous conditions and can be readily scaled for industrial purposes. There seems to be a lack of research on the spray-dry synthesis of mixed ferrites. Here, we provide a novel spray-drying method for producing CMF ferrite granules (Fig. 1a) with magnetic nanostructures. By gradually varying the Mn(II) with Co(II) in the system, we aim to fine-tune the saturation magnetization and inversion degree of the nanostructured $CoFe_2O_4$ ferrites granules on a massive scale. Both structural and magnetic characteristics are discussed to illustrate the impact of the replacement. Using the CMF system studied elaborately, we demonstrate that this method provides excellent size/-size distribution and yields magnetic nanocrystals with a stronger magnetic response while the synthesis approach itself is affordable, ecologically friendly, and more efficient.

2. Experimental details

2.1. Manufacturing of $Co_{1-x}Mn_xFe_2O_4$ (CMFO) micro-granules

The following raw materials and chemicals, which were purchased from Sigma Aldrich, were used in the manufacturing process of CMF materials. $Co(NO_3)_2{\cdot}6\ H_2O$, $Mn(NO_3)_2.4H_2O$, and $Fe(NO_3)_3{\cdot}9\ H_2O$, ethanol, and ammonia solution (25%). The compounds were utilized in their original form. Spray drying was used to create granules of $Co_{1-x}Mn_xFe_2O_4$. Metal precursors ((Co +Mn): Fe → (1:2)) and PEG-6000 (0.005 M) were dissolved in deionized water at stoichiometric molar ratios to produce a transparent solution; this was followed by the addition of ammonia (25% solution) to create a homogenous colloidal suspension that could be stored at room temperature (pH was kept at 10). A spray drier (dried length ~ 425 cm) in the lab was used to dry the colloidal solution (Labultima LU 228). We sprayed it with an ultrasonic spray nozzle. Aspiration rates of 45 m^3/hr were used to keep the input temperature at 140 °C. Throughout the trials, the vacuum was maintained at − 220 mm WC, and the feed pump flow rate was held at a steady 2–1 ml/min. The powder that was sprayed-dried was placed in a glass cyclone separator. It was discovered that the spray-dried powder was dark in color and quickly poured. The virgin powder was characterized after being annealed at 400 °C for an hour. $Co_{1-x}Mn_xFe_2O_4$ samples are conveniently denoted as CF, CMF1, and CMF2 for the values of x = 0.0, 0.1, and 0.2. Fig. 2 shows a representation of the synthesis process layout.

2.2. Characterization

D8-Advanced Bruker powder X-ray diffractometer (λ = 1.5406 Å) was used for structural analysis. The settings employed were: scan range of 20–80° (2θ range), 0.02° step size, and 0.4° scan rate per minute. The experimental X-ray diffraction (XRD) patterns were refined using the Rietveld structure method in Fullprof. By Fullprof Software, we are able to gather electron density maps in addition to calculating bond lengths and angles. The Rietveld method was used to generate the theoretical XRD patterns, which were based on data from the Inorganic Crystal Structure Database (ICSD) under code 109044. VESTA software program creates designs for the unit cell. Electron dispersive spectroscopy (EDS) was used to measure elemental quantification energy, and a scanning electron microscope (JEOL-JSM-6360) was used to examine the microstructural characteristics of pure microgranules. To decipher nanoscale structural information, we used small-angle x-ray scattering (SAXS) experiments in the lab. The scattered intensities I (q) were measured based on the scattering vector transfer ($q = (4\pi \sin\theta)/\lambda$), where θ is the scattering angle and λ is the x-ray wavelength (1.54 Å), and a mathematical model was fitted to the experimental scattering profile using SASFIT Software. The InVia Micro RAMAN (Renishaw) spectrophotometer was used for Raman research, and the 532 nm laser was used to conduct the experiments at room temperature. The Quantum Design Evercool II PPMS-6000 was used to detect magnetic M-H loops at 10 K and 300 K with magnetic fields up to 90 kOe. The temperature dependence of magnetization under an applied magnetic field of 100 Oe was investigated from 10 to 390 K using both zero-field cooling (ZFC) and field cooling (FC) approaches.

3. Results and discussion

3.1. Surface/Interface morphology, microstructure and internal structure

3.1.1. SEM and EDS

The pristine samples' morphology is shown in Fig. 3 at various magnifications. SEM micrographs show that all of the manufactured CF and CFM microgranules are spherical in appearance, despite some inevitable changes in granule size throughout the ultrasonic atomization process. However, a small percentage (1%) of hollow buckled [42,43] spherical particles have been discovered for the CF and CMF2 (see, Fig. 3d and k). To be clear, the drying rate in this scenario is far slower than it would be with an industrial spray drier and is thus insufficient. When the gas flow rate (45 m^3/hr) is divided by the cross-section of the drying chamber (diameter = 22.86 cm), the velocity (V_{gas}) of the carrier gas within the tube may be determined. Finally, we find that V_{gas} equals

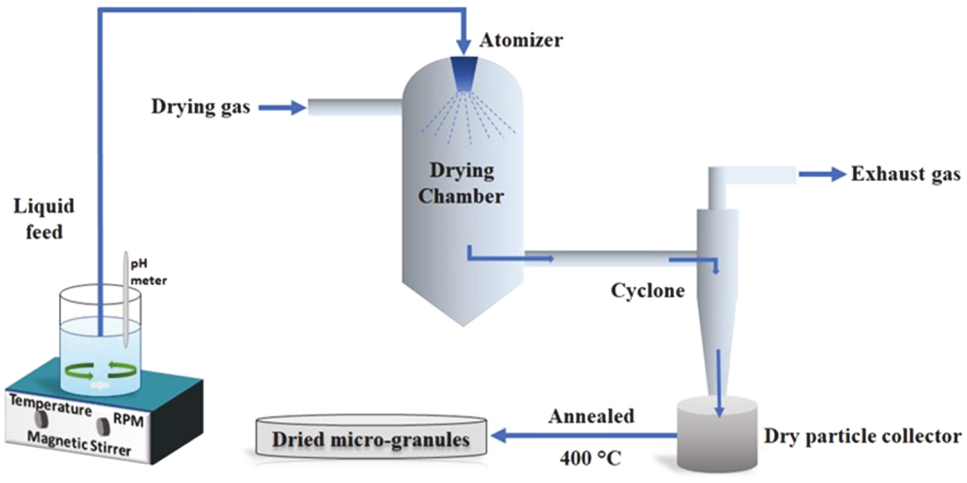

Fig. 2. Illustration of spray drying for $Co_{1-x}Mn_xFe_2O_4$ micro-granules.

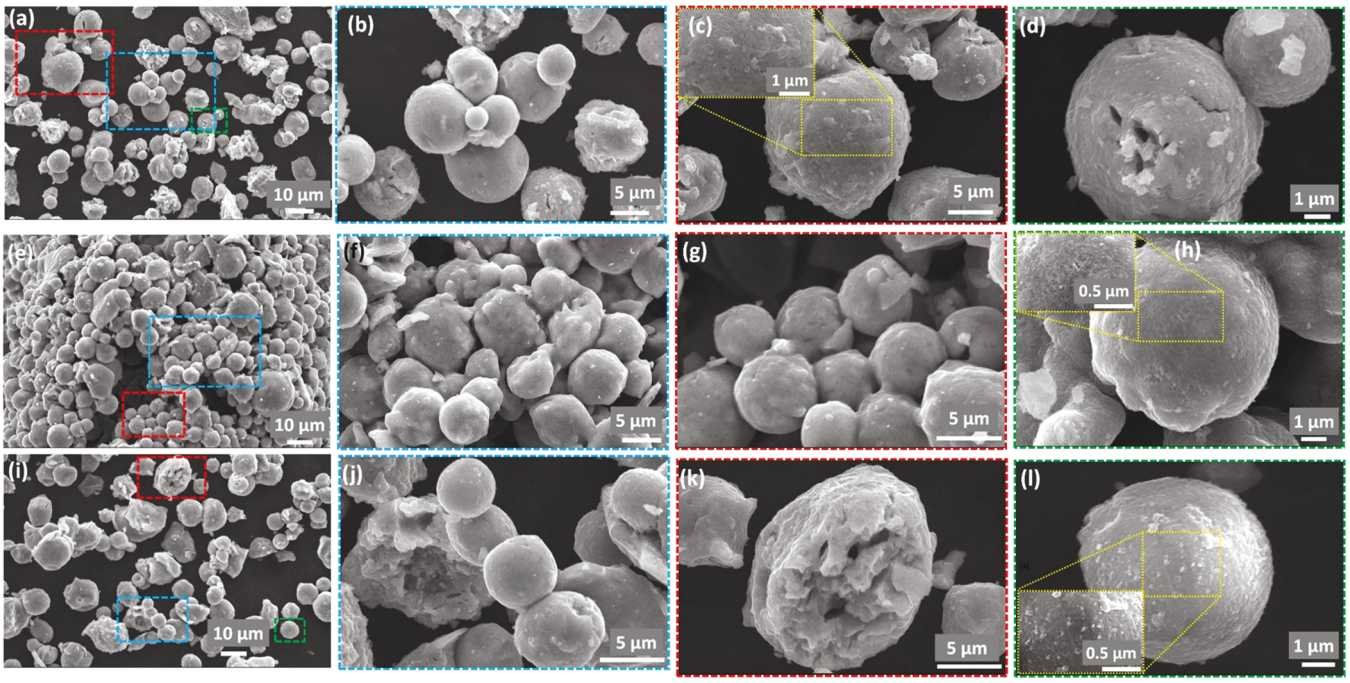

Fig. 3. SEM images of CF (*a* to d), CMF1 (e *to* h) and CMF2 (i *to* l) micro-granules at different magnifications.

18.28 cm/s. Drying time may be well estimated to be 23 s as droplets become dried at the end of the drying chamber, which is 425 cm in length; such a drying time corresponds to a slow drying regime or a non-buckling regime. It is important to note that this computation was performed to provide a rough estimate of the drying time. The speed within the tube may vary radially.

Fig. 3 shows that the self-assembled granules are perfectly spherical for all of the samples, which implies that the drying process is now operating in a non-buckling regime. Fig. 3(c, h, l) included enlarged micrographs that made the granules easier to see. Fig. 3(c, h, and l) also shows that compared to CF and CMF2, CMF1's subunit assemblies are somewhat fussed and organized compactly. One possible explanation is that CMF1 has a more excellent magnetic saturation value than CF and CMF2. The average size of the granules in CF, CMF1, and CMF2 is 6.55 ± 0.45, 6.14 ± 0.20, and 7.34 ± 0.41 μm, respectively. During the drying process of micrometric droplets containing a colloidal solution, droplet size reduction is driven mainly through evaporation. Due to the existence of wetting liquid between solid particles, capillary forces emerge, causing the component particles to combine due to attractive magnetic force. It has been reported [42] that when drying rates are low enough, droplets containing stable dispersions of colloidal nanoparticles shrink isotropically. The resulting configurations of the nanoparticles inside an assembled granule correspond to a packing owing to random jamming of the component particles. The formation mechanism of $Co_{1-x}Mn_xFe_2O_4$ micro-granules during spray drying is exactly as shown in Fig. 1(a).

In addition, EDS analysis of all samples is used to verify elemental quantification. Fig. S1 displays the EDS spectra that were acquired for all samples. The findings show that the target ratio of Co: Fe (1:2) is being maintained throughout all three samples, and the presence of Mn is measured to a significant degree in CMF1 and CMF2.

3.1.2. SAXS assessment

SEM micrographs could only reveal the granules' shape, not the nanoparticles' internal arrangements or correlations. As a result, SAXS was used to investigate all the samples. In order to establish a correlation between granule structure and nano-structured assemblies, the inter-particle structure factor was taken into account. Here, scattering data may reveal the inter-particle structure factor in terms of the correlation of interlocked nano-assemblies inside the granules and the precise nanostructure size distribution. Figures 4(a-c) demonstrates that the scattering patterns of CF, CMF1, and CMF2 samples are similar. The scattering intensity I(q), as a function of the wave vector transfer (q), was used to determine the presence of density fluctuations on the mesoscopic scale in a condensed matter system [44]. Scattering was approximated here by the sum of contributions from density changes in the whole granule and in the nano-entities that make it up.

Scattered information from samples with a q value between 0.1 and 0.3 nm^{-1} is attributed to the first region (Region I), while that from samples with a q value between 0.3 and 1.0 nm^{-1} is attributed to the second (Region II). The expression for the overall scattering intensity is:

$$I_{total}(q) = \sum_{i=1}^{2} I_i(q) = I_1(q) + I_2(q). \quad (1)$$

Scattering profiles of all samples have been examined using the polydisperse spherical particle model in the local-monodisperse approximation [39], which allows for an estimation of the size of the nano-structured entity and its modification with Mn substitution. The 'i^{th}' component's scattering contribution is denoted by 'I_i' here. The formula for the scattering intensity $Ii(q)$ is as follows:

$$I_i(q) = C_i \int_0^{\infty} P_i(q,R) S_i(q,R) R_i^6 D_i(R) dR. \quad (2)$$

C_i represents the scale factors, P_i (q, R) represents the form factors, S_i (q, R) is the structure factor, and D_i (R) is the size distribution for the i^{th} component of scattering intensity. Assuming the spherical shape of the particles with radius (R), Eq. (3) [45] expresses the form factor P_i (q, R). Assuming a normalized log-normal distribution, we get Eq. (4) [46] for $D_i(R)$:

$$P_i(q,R) = \left[\frac{3\sin(qR) - qR\cos(qR)}{(qR)^3}\right]^2. \quad (3)$$

$$D_i(R) = \frac{N}{\sqrt{2\pi\sigma^2}R} \exp\left[-\left[\ln(R/R_0)\right]^2 \Big/ 2\sigma^2\right] \quad (4)$$

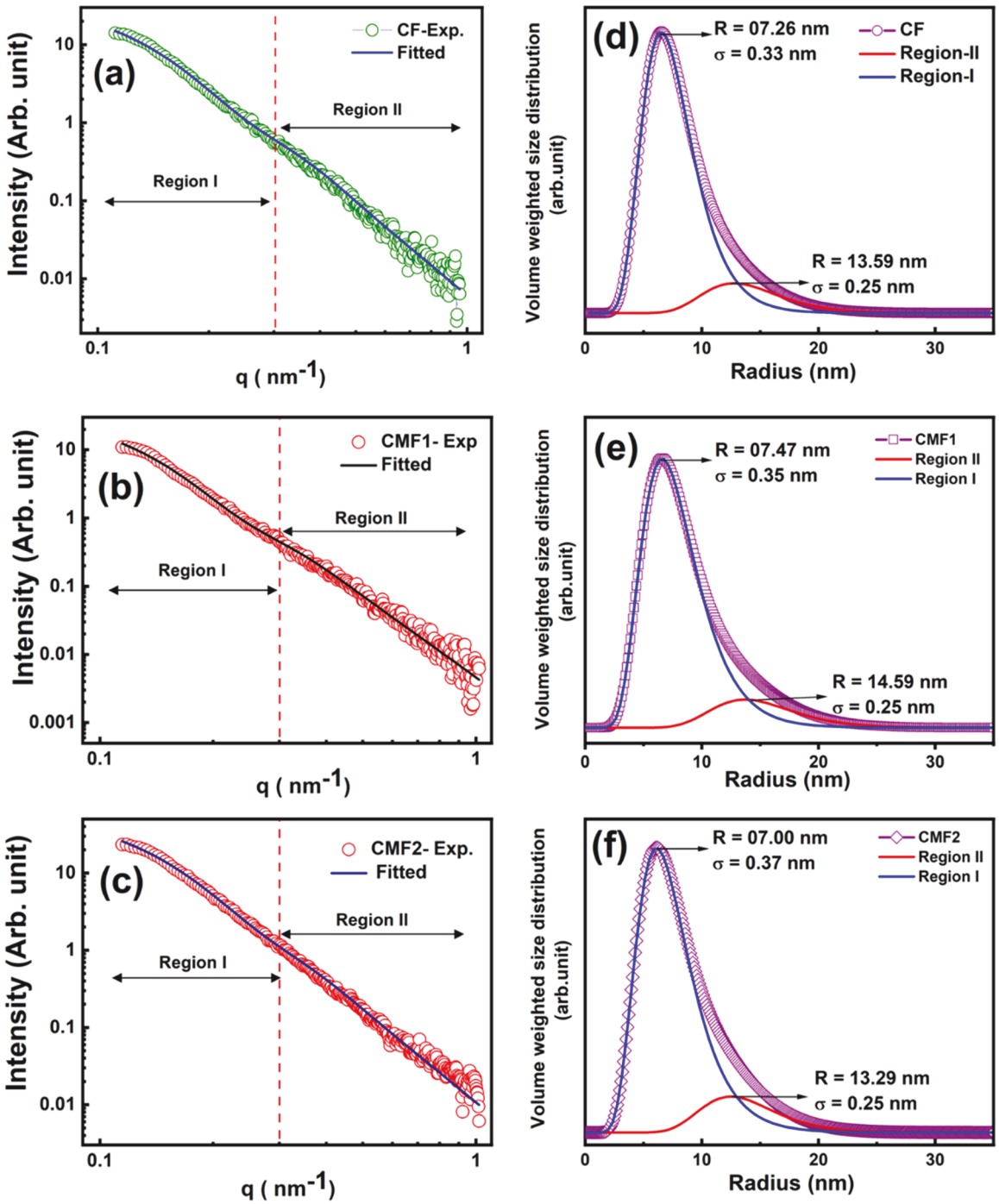

Fig. 4. SAXS profile for $CoFe_2O_4$ (a), $Co_{0.9}Mn_{0.1}Fe_2O_4$ (b), $Co_{0.8}Mn_{0.2}Fe_2O_4$ (c) micro-granules with a fitted mathematical model and the corresponding volume-weighted size distribution calculated are shown in (d), (e) and (f).

where N denotes a normalization factor, R_0 represents the median radius, σ indicates polydispersity index.

In this case, the magnetic interaction between the nano-spherical assemblies is crucial. Structure factor for sticky hard-sphere type potential [47] [48] with adjustable inverse stickiness parameter (τ) for area II is therefore included in Eq. (2) to account for the interparticle correlation in all three samples. Such a potential is analogous to a hard-sphere potential with a positive tail. A high value of 'τ' is analogous to a hard-sphere kind of contact, while a low value of 'τ' enhances the attractive contribution, resulting in more stickiness. All experimental profiles were fitted using Eq. (1). Fig. 4(a-c) shows the fitted SAXS

Table 1
Parameters obtained from the mathematical fitting to experimental small angle scattering profile; where R_o- median radius, σ - polydispersity index, τ-sickness parameter, and φ-volume fraction.

Sample	Region I	Region II	
CF	R_0 (nm) =13.59	R_0 (nm) =7.26	τ= 0.4
	σ (nm)=0.25	σ (nm)=0.33	φ=0.55
CMF1	R_0 (nm) =14.59	R_0 (nm) =7.47	τ= 0.35
	σ (nm)=0.25	σ (nm)=0.35	φ=0.58
CMF2	R_0 (nm) =13.29	R_0 (nm) =7.00	τ= 0.3
	σ (nm)=0.25	σ (nm)=0.37	φ=0.53

profiles. The model closely matches scattering data evolution. Table 1 lists the model-fitting estimates for the local volume fraction (φ), stickiness (τ), and structural characteristics of nano-structured. The stickiness of the nano-spherical entities is shown to drop from 0.4 to 0.3 as the Mn concentration rises. The volume percent is smaller for the CMF2 sample compared to the CMF1 and CF samples, and the value is smaller than unity for all three samples. These findings suggest that the nano-structured microgranules interact with one another in a manner like that of hard spheres. High-magnification SEM pictures further corroborate this by demonstrating how magnetic attractive contact strongly binds together fundamental nano-structure assemblies. As a result, secondary structure for an appealing potential form, leading to a rise in intensity in Region I. The volume weighted size distribution derived from the SAXS fit for all three samples is shown in Fig. 4(d-f). It is worth noting that the Fourier transform connects real space and scattering space, thus information regarding enormous length scales, such as secondary particles, and associated nano-structure entities at lower length scales may be found in the scattering profile's region-I and II, respectively. The effective volume weighted mean size distribution for CF is shown in Fig. 3(d); the median radius for region-I is R_{median} ~ 13.59 nm with a polydispersity index (σ) of 0.25, while the median radius for nanostructure recovered from region-II is R_{median} ~ 7.26 nm with a (σ) of 0.33 value. Fig. 4(d-f) shows that the secondary particles were restricted to a narrow diameter range, and that the nano-assemblies were only moderately polydispersed inside the granules.

3.2. Crystal structure, phase, and electron density

3.2.1. XRD and rietveld refinement

All XRD patterns were analyzed using the Rietveld refinement method [30]. All XRD patterns for $Co_{(1-x)}Mn_xFe_2O_4$ ($x = 0.0$–0.2) ferrites were refined to peaks in space group Fd3m with the following planes: (220), (311), (222), (400), (422), (511), (440), (620), (533), (622), and (444), demonstrating the development of a single-phase cubic spinel structure [30]. The XRD data of CF and CFM microgranules along with respective refinement data are presented in Fig. 5. As can be seen in Fig. 5(d), the (311) peak location is shifted toward lower 2θ for CMF1 and CMF2 compared to CF. Consequently, the equivalent lattice constant (a) varies as Mn concentration increases.

The peak profile of the XRD patterns was modelled using a pseudo-Voigt function with the oxygen positions as free parameters. All other atomic fractional positions, however, were considered as fixed values. Other factors, namely lattice constants, peak shape, and site occupancies were free parameters. Fig. 5 depicts observed and computed data, along with the difference between the two, so proving the acceptable fit of all samples. To preserve stoichiometry, the cation occupancy at tetrahedral and octahedral sites is restricted during the refinement of ferrites. According to Table S1, the resultant site occupancy factors are computed such that their total in A and B sites equals about one and two, which is compatible with the spinel ferrites formula AB_2O_4. The distribution of cations was calculated using the Rietveld refinement of occupancy values, and the results are shown in Table S1. This distribution reveals that regardless of the Mn content, all samples exhibit partially inverted spinel structures.

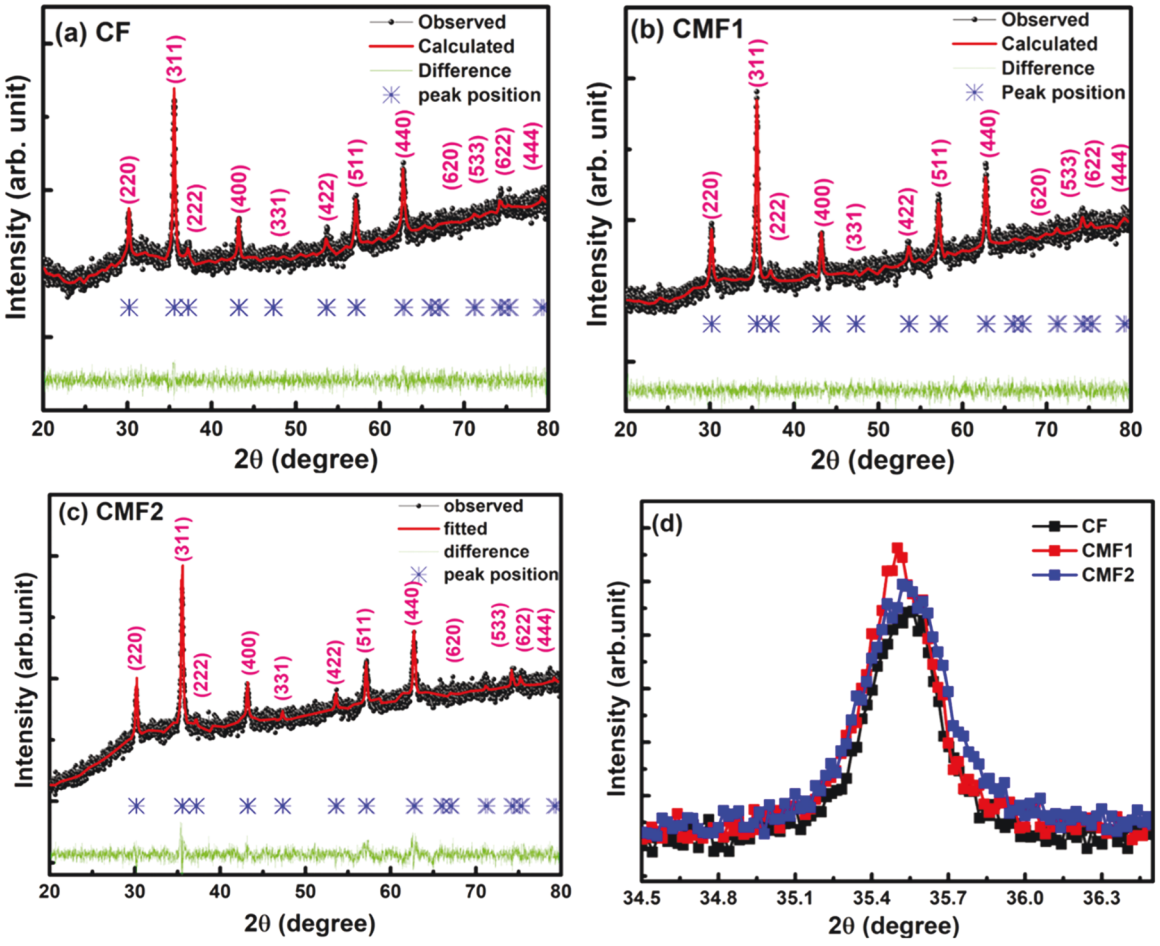

Fig. 5. Refined X-ray diffraction patterns of CF(a), CMF1(b), CMF2 (c) microgranules. And the enlarged diffraction plots for (311) peak for $Co_{(1-x)}Mn_xFe_2O_4$ samples (d).

Cationic stoichiometry usually affects the lattice constant in ferrites [5,49,50]. With increasing Mn content (x = 0.1), the lattice constant increases somewhat because Mn^{2+} (0.83 Å) ions replace Co^{2+} ions (0.78 Å) in the system [51], and these findings are in excellent agreement with the literature [36] [32]. Replacement of Mn^{2+} (0.83 Å) at the tetrahedral position by Fe^{3+} (0.49 Å) or Fe^{2+} (0.63 Å) and by Fe^{3+} (0.64 Å) or Fe^{2+} (0.78 Å) at the octahedral site may be responsible for the same effect in CMF2.

Cubic spinel ferrite's magnetic interaction strength is determined by the estimated cation-cation bond length, as well as the cation-anion bond length and bond angle [52]. Table S2 shows the results of all the calculations for bond lengths and bond angles. The cation-oxygen bond

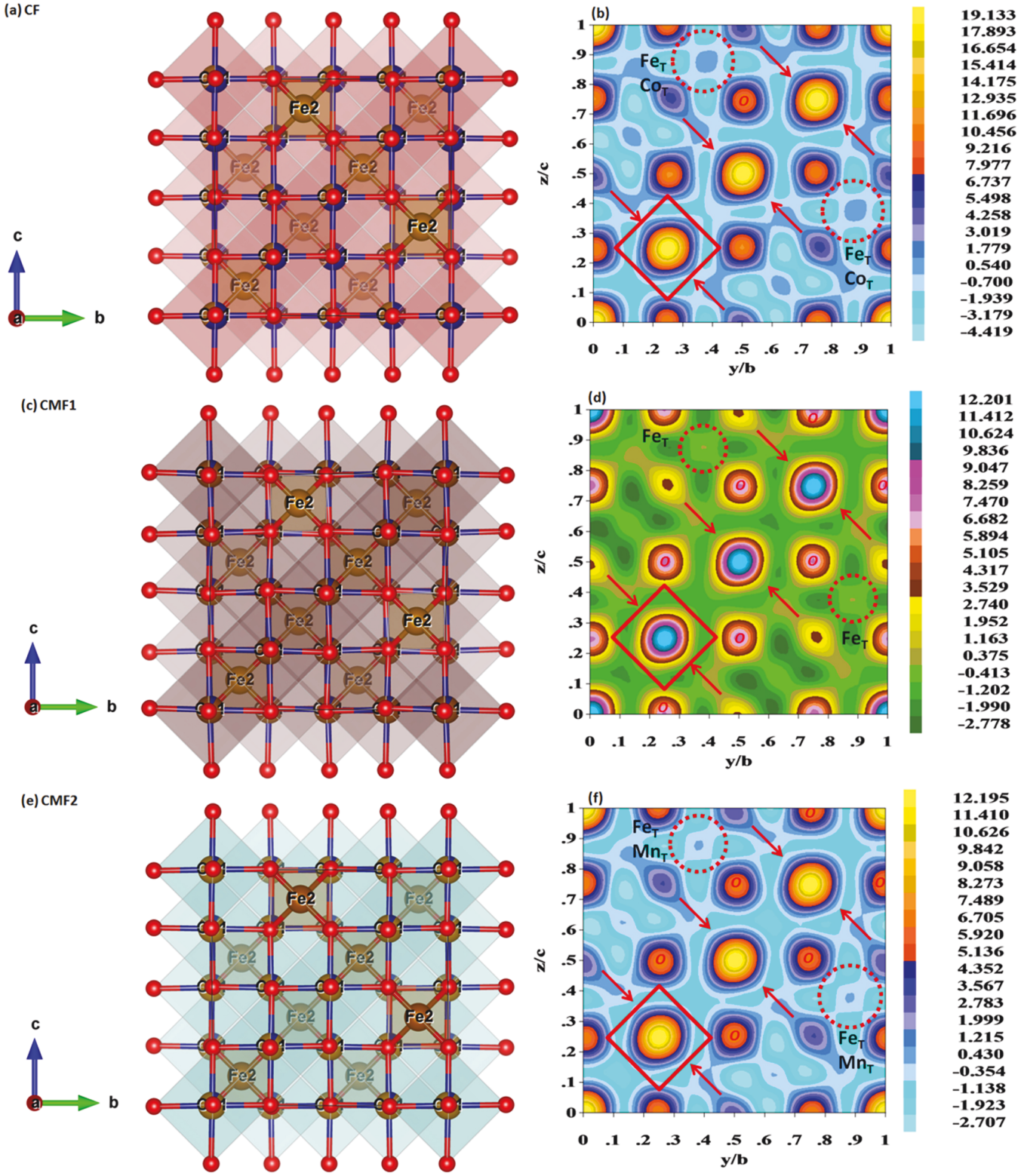

Fig. 6. The electron density plots in the *yz*-plane taken at an *x* intercept of zero ($x = 0$) for CF (b), CMF1 (d) and CMF2 (f) along with the corresponding section of unit cell (a, b, and c).

length in CMF1 is 2.147 Å, which is longer than that in CF (2.075 Å) and CMF2 (2.063 Å) at the octahedral location. While the cation-oxygen bond length is shorter (1.722 Å) in the tetrahedral site of CMF1, it is longer (1.865 Å) and (1.845 Å) in the tetrahedral sites of CMF2 and CF, respectively.

Table S2 demonstrates without a doubt that all samples have an O-Fe2-O bond angle that is identical to the spinel value of 109.47°. Furthermore, for CMF1, the O-Co1-O and O-Mn1-O bond angles deviate to 87.22° at the octahedral site, but the O-Fe1-O bond angle deviates to 92.78° from the ideal spinel value of 90°. Additionally, the bond angle values between the $(cation)_{octahedral\ site}$-oxygen-$(cation)_{tetrahedral\ site}$ in CF, CMF1, and CMF2 are 124.53°, 127.25°, and 124.07°, respectively, which is somewhat off from the ideal spinel value of 125°. CMF1 exhibits substantial local octahedral distortion, which is consistent with a replacement of Co^{2+} (0.78 Å) for Mn^{2+} (0.83 Å) at an octahedral site. In this way, the buckles of the FeO_6 and CoO_6 octahedra caused by the substitution of Mn^{2+} ions are shown by the notable deviation in the Co1-O-Fe2 and Fe1-O-Fe2 bond angle. The well-known antiferromagnetic A-B interaction may be affected by this skewed angle. The O-Co1-O and O-Fe1-O bond angles measured for CF and CMF2 samples are likewise slightly off from the ideal spinel value of 90°, at 91.05° and 91.71°, respectively. When Mn^{2+} is replaced at the octahedral and tetrahedral sites in CMF2, the bond lengths of the Mn1-O atoms are elongated to 3.471 Å from CF and CMF1 samples, while the Fe2-O atoms are shortened to 2.063 Å. Therefore, we have projected that the antiferromagnetic A-B interaction for CMF2 should be lower than for CF and CMF based on observed values of bond angles and bond lengths in all three samples. In this way, CMF2 has a lower saturation magnetization than CF and CMF1.

Examining bond lengths and angles indicates that the whole composition tends to stabilize in a cubic form with no tetrahedral distortion. However, Co and Mn cations cause a slight local deformation at the octahedral location.

3.2.2. Electron density mapping

The electron density graphs help better clarify the distortion caused by the Mn replacement. In order to comprehend the interactions at the molecular level, electron density maps are crucial. Inverse Fourier transformation of the structure factors F_{hkl} obtained from the Rietveld refinement gives the electron density $\rho(x, y, z)$ as [53]:

$$\rho(x,y,z) = \sum_{hkl} \frac{F_{hkl} \rightleftarrows e^{[-2\pi i(hx+ky+lz)]}}{V} \ldots\ldots\ldots \quad (5)$$

where (h, k, l) are the Miller indices and V is the volume of a unit cell. Because CF, CMF1, and CMF2 occupy separate sub-lattices, the electron density map reveals that the quality of the tetrahedral "A" sites and the octahedral "B" sites are distinct. This is due to the inversion of the structures of CF, CMF1, and CMF2, as well as the substitution of Co^{2+} for Mn^{2+}. Unit cell sections matching to all three samples are shown in the leftmost column of Fig. 6. We have cut the unit cells in such a way that the disparities between the electron concentrations in the octahedral yz-plane and the tetrahedral sites are readily apparent. Octahedral site cation (Co1, Fe1) yz-plane at $x = 0$ and O^{-2} ion interactions are shown well (octahedral site electron cloud is shown by arrow arranged diagonally). Cation-oxygen bonds at the B site appear in the yz plane to create a cube with a central cation (Co1 or Fe1) and vertices made up of oxygen ions (red solid cubic drawn as a guide to the eye). Even though the particle size is different for CMF1 and CMF2 compared to CF, the oxygen atoms are still organized in a cube with a diagonal in the yz plane, however the cation-oxygen Co1-O bond length shifts as mentioned above. Fig. 6 further demonstrates that the octahedral site has a greater electron density distribution than the tetrahedral site across all three samples. Please refer to Fig. 6 where the tetrahedral location is highlighted in red. This may be interpreted as follows: because electron clouds are the root cause of diffraction, we can assume that the larger the predicted atomic number of elements, the more massive the electron cloud will be. So, the presence of Mn^{2+} with the Co^{2+} and Fe^{3+} dominates in the CMF2 sample, as shown by the greater electron density cloud detected at the B site compared to the CMF1 and CF samples. When comparing CMF2 and CF to CMF1, the electron density cloud order at the A site suggests the existence of Mn^{2+} and Co^{2+} in addition to Fe^{3+}. Moreover, it is also found that the three samples have slightly different bond angles from ideal values at the B site, which leads to a little anisotropy in electron density (deviated spherical electron cloud). This study of particles of variable sizes and cation distributions contributes to our knowledge of the variations in magnetic characteristics reported in CF, CMF1, and CMF2 samples.

3.3. Chemical bonding

3.3.1. Raman spectroscopy

Raman spectroscopy, a supplementary approach for structural characterization [54], was used to describe samples further to expose the influence of Mn substitution in $CoFe_2O_4$ microgranules. Fig. 7 shows the Raman spectra of the CF and CMF1 samples, and Table 2 summarizes the Raman modes. Five Raman active phonon modes, characteristic of spinel-type cubic ferrites in the *Fd3m* space group, can be seen in both spectra, including $A_{1\,g}$, 3 $T_{2\,g}$ and E_g. The lack of other modes confirmed the samples' excellent phase purity. $A_{1\,g}$ symmetry, including symmetric stretching of oxygen ions with respect to metal ions in a tetrahedral void, is responsible for the peaks at 687 cm^{-1}. The metal ion produces phonon modes E_g and 3 $T_{2\,g}$ below 600 cm^{-1} in an octahedral void. These

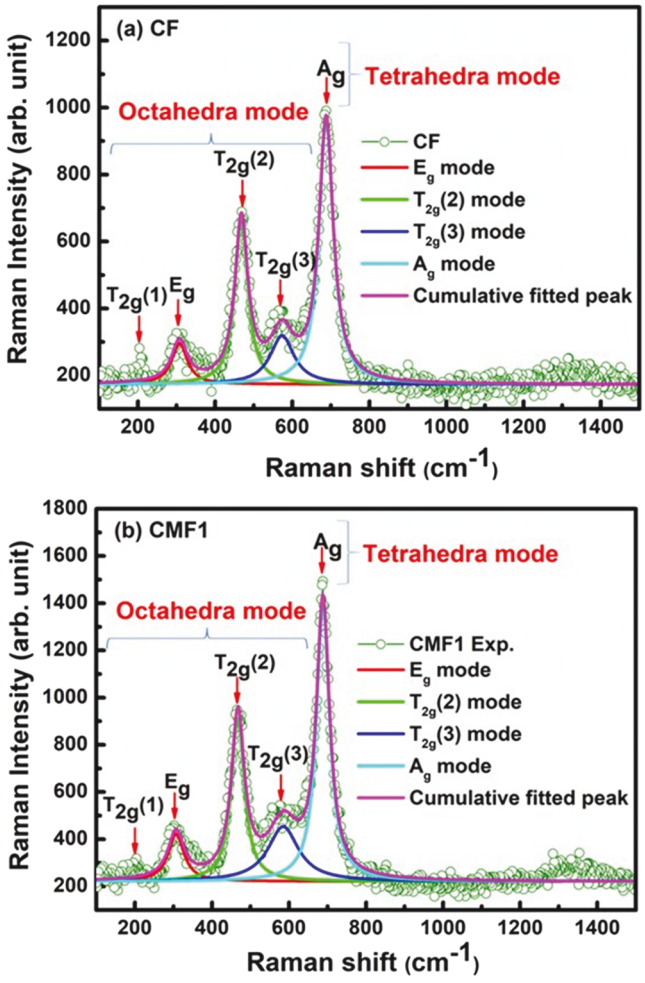

Fig. 7. Raman spectra for CF (a) and CMF1 (b) micro-granules captured at room temperature.

Table 2
Raman parameter summary.

Sample	Peak position (cm^{-1})	FWHM (cm^{-1})	Area (cm^2)	Intensity	Raman active mode	Assigned Polyhedra
CF	307.52 ± 1.60	49.18 ± 4.81	9501.85 ± 696.18	122.99	E_g	FeO_6 Octahedra
	468.08 ± 0.37	41.16 ± 1.24	31366.54 ± 778.61	485.09	$T_{2\,g}(2)$	
	573.56 ± 1.78	74.95 ± 6.67	17097.32 ± 1249.08	145.21	$T_{2\,g}(3)$	
	687.71 ± 0.24	45.16 ± 0.78	55686.19 ± 790.64	784.98	A_g	FeO_4 tetrahedra
CMF-1	306.86 ± 1.29	49.94 ± 3.89	15763.36 ± 922.48	200.96	E_g	FeO_6 Octahedra
	467.22 ± 0.34	41.20 ± 1.17	44678.13 ± 1082.96	690.29	$T_{2\,g}(2)$	
	584.74 ± 1.79	96.65 ± 7.31	35264.50 ± 2302.28	232.27	$T_{2\,g}(3)$	
	687.91 ± 0.20	41.23 ± 0.72	75520.59 ± 1197.22	1165.98	A_g	FeO_4 tetrahedra

vibrational patterns reflect the symmetric and anti-symmetric bending in the M-O bond when oxygen ions occupy octahedral vacancies. The Raman spectra of CMF1 display a minor blue shift in peak position for $T_{2\,g}(3)$ and A_g mode and a slight red shift in peak position for E_g and $T_{2\,g}$ (2) mode compared to CF. A possible explanation is that Co and Mn have a greater mass at the octahedral position than Fe. Furthermore, when comparing the FWHM of CF and CMF1, the FWHM of the octahedral site peak expanded, whereas the FWHM of the tetrahedral mode peak declined. The presence of Co^{2+} and Mn^{2+} cations is thought to cause local disorder, which in turn causes the octahedral mode to expand. The shift in bond length and angle further supports it.

Furthermore, the area ratio of tetrahedral to octahedral mode peak, i.e., $A_g/T_{2\,g}$ (3), $A_g/T_{2\,g}$ (2), and A_g/E_g, is found to be (3.26, 1.78, 5.86) and (2.14, 1.69, 4.79) for CF and CMF1, respectively. The intensity ratio of tetrahedral to octahedral mode peak, i.e., $A_g/T_{2\,g}$ (3), $A_g/T_{2\,g}$ (2), and A_g/E_g is found to be (5.41, 1.62, 6.38) and (5.02, 1.69, 5.80) for CF and CMF1, respectively. With Mn substitution, the area and intensity ratio of tetrahedral to octahedral mode decreases. Overall, the change in the area, FWHM, and intensity of the Raman active mode suggest a progressive increase in the degree of inversion of the spinel lattice. In addition, this suggests the cation migration within both positions. Similar behaviour was observed for the CMF2 sample (not shown here).

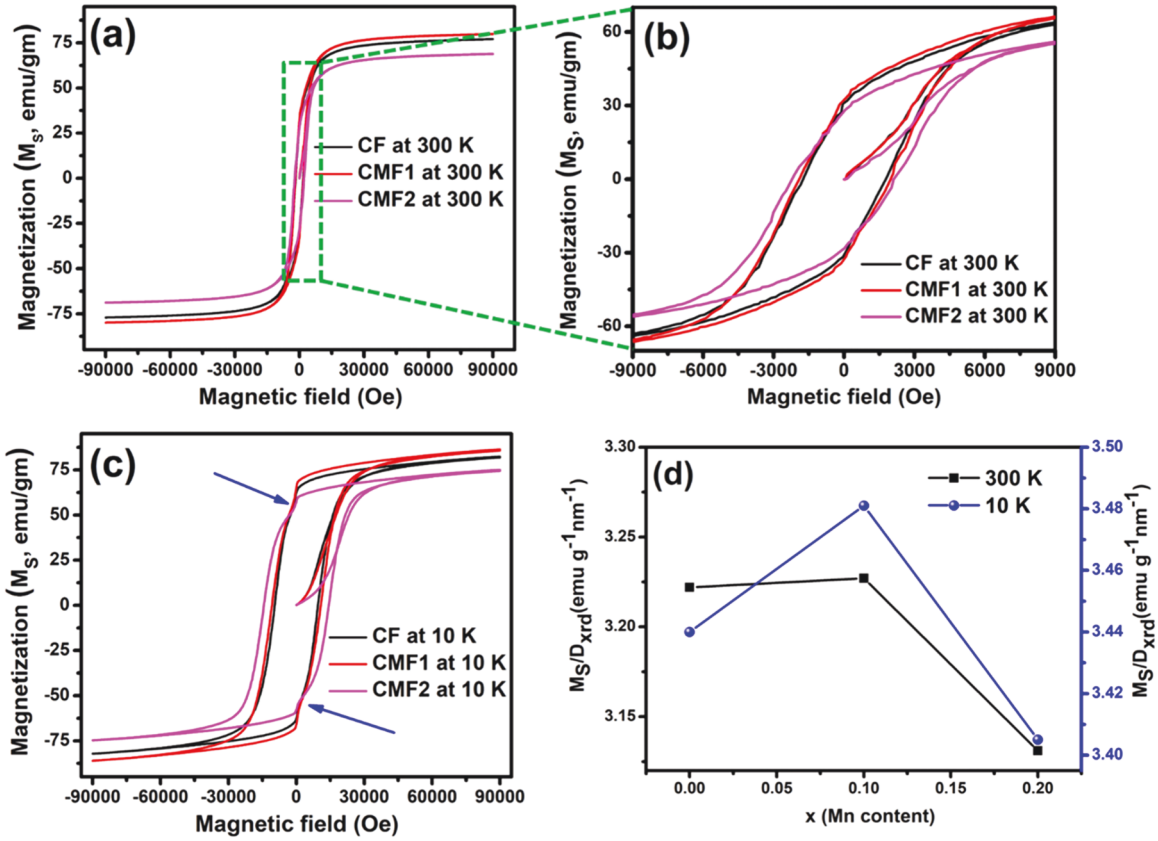

Fig. 8. M-H curve at 300 K (a), along with the magnified plot, (b) M-H curve at 10 K, (c) and M_S/D_{xrd} measured at 300 K and 10 K as a function of Mn content for Co_{1-x} $Mn_xFe_2O_4$ samples.

3.4. Magnetic property and performance evaluation

The magnetization dependence of the DC magnetic field M-(H) hysteresis loops of the Co_{1-x} $Mn_xFe_2O_4$ microgranules, measured at 300 K and 10 K in the magnetic field ranging from − 90 kOe to + 90 kOe, is presented in Fig. 8(a,b) and (c). The magnetic parameters obtained from the M-(H) hysteresis loops of the Co_{1-x} $Mn_xFe_2O_4$ microgranules, are listed in Table 3. The existence of a well-defined magnetic hysteresis loop at 10 K, as well as the enlarged image of M-(H) hysteresis loops (Fig. 8(b)), reveals the long-range ferromagnetic behavior of the Co_{1-x} $Mn_xFe_2O_4$ microgranules. At 300 K, maximum saturation magnetization (M_S) values are 77.05, 79.87, and 68. 89 emu/gm for CF, CMF1, and CMF2, respectively. It is important to note that the M_S value observed for CF microgranules is close to the bulk CFO (80 emu/g) and higher than the M_S value reported for nano/microscale CF at the same experimental conditions [18,30,55].

For x = 0.1 Mn substitutions, M_S and M_r values improved for CMF1 compared to CF microgranules at 300 K and 10 K. However, the M_S and M_r value fall in comparison to CF when Mn content rises more. Here, an increase in M_S value for CMF1 is due to the substitution of high (5 μ_B) magnetic moment Mn^{2+} for low (3 μ_B) magnetic moment Co^{2+}. Magnetic characteristics in the ferrite system are significantly affected by the site preference of cations in the spinel lattice [56], in addition to exchange interactions between the magnetic ions residing at B and A sites. Over-oxidation of the Mn ions increases the likelihood of Mn ions occupying octahedral sites [57] and raising the valence of Mn ions from 2 + , 3 + , and 4 + reduces the total magnetization. If Mn is present in larger quantities (i.e., x = 0.2), it will be replaced as Mn^{2+} (5 μ_B) and Mn^{3+} (4 μ_B). Then, the magnetization is predicted to drop as Fe^{3+} (5 μ_B) is reduced to Fe^{2+} (4 μ_B). Thus, M_S value variation with Mn substitution is ascribed to the magnetic moment contributions at the A-site and B-site of the spinel ferrite. Moreover, their corresponding decrease in magnetocrystalline anisotropy of Co with the Mn substitution.

Additionally, the magnetic characteristics are sensitive to variations in particle size, cation distribution, exchange couple interaction, and surface area/volume ratio. Therefore, the M_S/D_{xrd} values should be compared for an accurate reflection of the variations in magnetic properties among nano-structured microgranules. Fig. 8(d) displays the M_S/D_{xrd} values as a function of x determined in this study at temperatures 300 K and 10 K. (d). CMF1 has the most significant M_S/D_{xrd} values, and the findings follow a similar pattern.

Consistent with prior research [58], we also found that the M_S, M_r, and H_C values of all the microgranules samples were significantly higher at 10 K than those obtained at 300 K. This spin structure consists of a spin-ordered core and a spin-disordered shell owing to either spin canting or surface anisotropy [59]. It is likely responsible for the observed rise in M_S at 10 K for nano-structured granules. In this investigation, however, the size of nano-structured micro-granules, as well as the simultaneous impact of spin disorder (or spin canting), effective anisotropy, and interaction among the NPs, all play essential roles. It is noteworthy that none of the three samples thoroughly saturate in magnetization at 10 K, despite having done so at 300 K. At the nanoscale, this is ascribed to spin canting at the particle surface [60], and it is a characteristic hallmark of magnetism in CF-based materials. Surface spins at 10 K are not perpendicular to core spins but are skewed away from the anisotropy axis of the particles.

Furthermore, an extra kink (depicted by the arrow in Fig. 8(c)) is found in the M (H) curve for all samples at 10 K. Kinks in the M (H) loop emerge owing to magnetic exchange coupling between the hard-soft phases of the material, spin reorientation of the surface spine, and interparticle interactions, according to the literature [61]. However, in the current investigation, all samples are single-phase, as confirmed by XRD and Raman spectroscopy. As a result, the magnetic exchange interaction between the hard and soft phases is ignored. The observed kink in M(H) loops at 10 K may be attributed to surface spin reorientation, domain wall pinning, and interparticle interaction. Because morphological SEM images and SAXS analysis evidenced that the microgranules are made of the primary NPs and making the magnetic coupling stronger, thus presence of surface spin reorientation, domain wall pinning, and interparticle interaction is quite reasonable and can justify the presence of kink in M(H) loops at 10 K.

The nano-structured CF granule has a coercivity (H_C) at 10 K of 9.54 kOe, which is a much higher value than bulk CFO (∼5 kOe at 5 K) [60],[62]. It was also shown that the coercivity of the Co_{1-x} $Mn_xFe_2O_4$ system increased from x = 0 to x = 0.2. In this regard, the H_C/D_{XRD} and H_C/D_{SEM} values as a function of x were determined (not shown). The results follow similar trends, with $Co_{0.8}Mn_{0.2}Fe_2O_4$ presenting the highest H_C/D_{XRD} and H_C/D_{SEM} values at 10 K. This is in line with previous reports that the particle size of MNPs monitor the coercivity. Particle size distribution, morphology, surface spin, and interparticle interactions all have a role in determining the H_C. However, in the current investigation, the primary elements that determine H_C are the effective anisotropy, the various exchange-couple interaction, and the interactions between the nanostructure. Because of this, the high-field area (40–90 kOe) of the M-(H) curve was carefully studied for all samples. Smaller magnetization-field effects are often seen in the high-field area, where domain rotation is the primary influence. For a polycrystalline magnetic material, the relation between 'M' and 'H' in this area is often expressed as, which is referred to as the "law of approach" to saturation [63].

.

$$M(H) = M_S\left(1 - \frac{a}{H} - \frac{b}{H^2} - .....\right) + \chi_P H.... \quad (6)$$

where M(H) is the magnetization at applied field (H), M_S is the saturation magnetization and term χ_pH denote the field-induced increase in the spontaneous magnetization of the domains, or forced magnetization. This factor is beneficial at high temperatures and high fields. This component is negligible at temperatures below the Curie temperature (T_c) (for bulk CFO, T_C = 798 K); hence it may be disregarded in the current investigation [64]. The term a/H is attributed to the strain field around dislocation in the material [64]. Eq. (6) may be expressed in two more ways:

$$M(H) = M_S\left(1 - \frac{b}{H^2}\right)..... \quad (7)$$

$$M(H) = M_S\left(1 - \frac{a}{H} - \frac{b}{H^2}\right)..... \quad (8)$$

First, a test fit was performed using Eqs. (7) and (8) by adjusting the

Table 3
Summary of magnetic parameters obtained from M-(H) hysteresis loops of the Co_{1-x} $Mn_xFe_2O_4$ microgranules at 300 K and 10 K temperatures.

Sample	Saturation magnetization (M_S, emu/gm)		Saturation magnetization (M_S, μ_B/F.U)		Remanent magnetization (M_r, emu/g)		Coercivity (H_C, KOe)		Squarness Ratio (M_r/M_s)	
Temperature	300 K	10 k	300 K	10 k	300 K	10 k	300 K	10 k	300 K	10 k
CF	77.05	82.27	3.237	3.456	30.9	62.47	1.76	9.54	0.401	0.759
CMF-1	**79.87**	**86.18**	**3.350**	**3.614**	32.53	65.61	1.96	10.80	0.407	0.761
CMF-2	68.89	74.1	2.884	3.102	27.98	57.54	2.16	14.35	0.406	0.777

minimum field limit to more than 40, 60, and 70 kOe while maintaining the maximum field at around 90 kOe. This was done to find the best field range where the law of approach can be used. Fig. S3 (a, b, c) and (d, e, f) show a test fit for all the samples using Eq. (7) at 300 K and 10 K, respectively. Statistical parameters give information on applying the law of approach to saturation over the varied range of the applied field in this instance. Table 4 contains the fitting parameters. Intriguingly, it was discovered that the statistical parameters, namely the χ^2 and R^2 values, varied depending on the initial magnetic field. It is evident that both values improve immensely with increasing lower fields. In addition, the values of χ^2 and R^2 for 70 kOe are deemed ideal. Table 4 indicates that when the value of M_S rises, statistical metrics improve. The lower magnetic field limit for Eq. (7) is determined to be more than 70 kOe based on these studies.

Table 5 enlists all the parameters obtained from Eq. (8) fitting. In the prepared microgranules, Eq. (7), χ^2 and R^2 values are best for a lower limit above 60 kOe. Similarly, Fig. S4 (a–c) and (d–f) show the results of a test fitting for all the prepared samples using Eq. (8) at 300 K and 10 K, respectively. It also indicates that the contribution of (a/H) to variations in the statistical parameters characterizing the dependence plays a vital role. Therefore, the current research finds the minimal field based on the optimal range predicted by statistical characteristics. In the case of Eq. (7), for the magnetic field range 70 < H < 9,0 kOe, the value of M_S and *b* increases for $x = 0.1$ while both values decrease with increasing concentration of Mn. Similarly, improving values of *a* and *b* were observed at the $x = 0.1$ for Eq. (8) in the 60 < H< 90 kOe magnetic field range. Eq. (7) fitting to experimental data shows the negative value of *b*. This negative number lacks considerable particular value [65].

Typical fittings for the CF, CMF1 and CMF2 are shown in Fig. 9(a), (b), and (c), respectively, using Eqs. (7) and (8) at 300 K. In the applied magnetic field 40 < H < 90 kOe, the equation comprising 1/H and $1/H^2$ components provided the best fit to the curve. Magnetization is discovered to be a function of 1/H and $1/H^2$ for all samples within the same field range. In addition, it is evident that the elimination of the 1/H term reveals the changes in the statistical characteristics, indicating the importance of each term to characterizing the dependence. In addition, the following relationship exists between coefficient *b* and K_E [64]:

$$b = \frac{4K_E^2}{15.M_S^2} = \frac{4.\left(K_{Sh}^2 + K_{St}^2 + K_{Sf}^2 + \frac{2}{7}K_1^2\right)}{15.M_S^2}..... \quad (9)$$

where K_{Sh} *is* shape anisotropy, K_{St} *is* stress anisotropy, K_{Sf} *is* surface anisotropy, and K_1 is magnetocrystalline anisotropy. The parameters '*b*' and 'M_S,' obtained through fitting Eqs. (7) and (7), are used to determine K_E at 10 K and 300 K in the corresponding best-fitted applied region. The values of K_E are summarized in Tables 4 and 5. Notably, the K_E value of nano-structured CF granules is more significant (11.1×10^7 and 15.21×10^7 erg/cm^3) than that of CF NPs prepared by another method (9.90×10^6 erg /cm^3 at 10 K) [66] and that of bulk CFO ($1.8–3.0 \times 10^6$ erg/cm^3 at 300 K) [60]. In addition, with a decrease in temperature from 300 K to 10 K, the K_E value increases for all three samples. The high H_C and K_E values are believed to result from the surface anisotropy of canted spins at the NP surface [66].

The ZFC and FC magnetization curves for all samples are shown in Fig. 10. Qualitatively, all samples are very similar: From 390–39 K (at 100 Oe), the FC magnetization decreases monotonically; this corresponds to a non-interaction zone; below 39 K, the magnetization displays almost saturated behavior, exhibiting temperature independence. Possible causes include the size-dependent effects of dipolar and interparticle coupling interactions [18]. The blocking temperature is the temperature at which cups define the ZFC curve of NPs (T_B). Materials exist in a superparamagnetic state at T_B with about 0% H_C, whereas a hysteresis loop is seen below T_B. Here, the maximum (T_{max}) M_{ZFC} temperature occurs at 390 K and climbs as the temperature increases. Furthermore, increasing volume anisotropy and interparticle interaction may cause T_{max} to shift to higher temperatures [67]. $T_{max} = AT_B$, where A is a number between 1 and 2.73, is a first-order estimate for the connection between T_{max} and T_B. According to the results of this study, T_B is about 390 K. The comparatively higher T_B may be explained by the high anisotropy of $Co_{1-x}Mn_xFe_2O_4$ samples [18,58]. Thus, at 390 K, $Co_{1-x}Mn_xFe_2O_4$ samples are superparamagnetic, as shown by ZFC and FC at 100 Oe. As can be shown in Table 3, the squareness ratio of samples at 10 K is much higher than the 0.68 at 5 K, 0.75 at 5 K and 0.6 at 10 K reported earlier [68,69,70]. However, for non-interacting single-domain particles with arbitrarily oriented easy axes, R is 0.5 for uniaxial anisotropy and 0.832 ($K_1 > 0$) or 0.87 ($K_1 > 0$) for cubic anisotropy [70,71]. As a result, the observed values of cubic anisotropy at 10 K are quite close to the predicted value. Furthermore, the R-value predicts the presence of different inter-grain group exchanges; for R < 0.5, the particles can interact via magnetostatic interaction; for R = 0.5, randomly oriented non-interacting particles undergo coherent rotations [18], and 0.5 < R < 1 confirms the existence of exchange-coupling particles. Thus, at 300 K and 10 K, the sample particle interaction is analogous to the magnetostatic and exchange coupling interactions between grains.

4. Conclusions

We present a detailed and exploration study, which is the very first report to the best of authors' knowledge, of the spray drying-based

Table 4

Adj. R-Square, Ms (emu/g), b (Oe^2), K_E (erg/cm^3) derived from the curve fitting using $M(H) = M_S\left(1 - \frac{b}{H^2}\right)$ at various field areas for varied concentrations (x) of $Co_{1-x}Mn_xFe_2O_4$ microgranules at 300 K and 10 K.

Sample	Field range 40,000 < H < 90,000 Oe			Field range 60,000 < H < 90,000 Oe			Field range 70,000 < H < 90,000 Oe			
	χ^2, R^2	M_S	*b* ($\times 10^7$)	χ^2,R^2	M_S	*b* ($\times 10^7$)	χ^2, R^2	M_S	*b* ($\times 10^7$)	K_E ($\times 10^6$)
At 300 K										
CF	0.0109	77.49	06.22	0.0007	77.90	08.91	0.00013	78.06	10.20	8.42
	0.97475	± 0.01	± 0.60	0.99203	± 0.00	± 0.62	0.99618	± 0.00	± 0.60	
CMF1	0.00869	80.33	05.66	0.00057	80.69	07.96	9.36×10^{-5}	80.83	09.07	9.12
	0.9772	± 0.01	± 0.53	0.99291	± 0.00	± 0.53	0.9969	± 0.00	± 0.49	
CMF2	0.00832	69.29	06.56	0.00056	69.64	09.17	8.66×10^{-5}	69.78	10.46	8.44
	0.97815	± 0.01	± 0.58	0.99293	± 0.00	± 0.59	0.997	± 0.00	± 0.54	
At 10 K										
CF	0.1030	83.06	17.15	0.0066	84.31	24.68	0.00088	84.78	28.15	15.21
	0.97212	± 0.04	± 0.16	0.99215	± 0.02	± 0.16	0.99721	± 0.01	± 0.13	
CMF1	0.10129	86.95	17.50	0.00498	88.17	24.53	0.00060	88.59	27.43	17.41
	0.97607	± 0.04	± 0.15	0.99444	± 0.02	± 0.13	0.99811	± 0.01	± 0.10	
CMF2	0.07429	75.75	19.36	0.00351	76.79	26.13	0.00043	77.13	28.90	15.51
	0.98151	± 0.03	± 0.15	0.99549	± 0.02	± 0.13	0.99844	± 0.01	± 0.10	

Table 5

Adj. R-Square, Ms (emu/g), *a* (Oe), b (Oe^2) derived from the curve fitting using $M(H) = M_S\left(1 - \frac{a}{H} - \frac{b}{H^2}\right)$ at various field areas for varied concentrations (*x*) of $Co_{1-x}Mn_xFe_2O_4$ microgranules at 300 K and 10 K.

Sample	Field range 40,000 < H < 90,000 Oe				Field range 60,000 < H < 90,000 Oe					Field range 70,000 < H < 90,000 Oe			
	χ^2, R^2	M_S	*a*	*b* ($\times 10^7$)	χ^2, R^2	M_S	*a*	b ($\times 10^7$)	K_E ($\times 10^6$)	χ^2, R^2	M_S	*a*	b ($\times 10^7$)
					At 300 K								
CF	6.62×10^{-5}	79.65	3268.08	-03.27	1.17×10^{-5}	80.09	4040.48	-06.00	6.46	1.08×10^{-5}	80.36	4561.50	-08.10
	0.99985	± 0.01	± 15.32	± 0.44	0.99987	± 0.02	± 39.82	± 0.14		0.99969	± 0.06	± 129.40	± 0.51
CMF1	4.76×10^{-5}	82.24	2806.83	-02.47	6.62×10^{-6}	82.61	3416.87	-04.63	6.52	5.76×10^{-6}	82.75	3680.35	-05.67
	0.99987	± 0.00	± 12.74	± 0.37	0.99992	± 0.01	± 29.14	± 0.10		0.99981	± 0.04	± 91.12	± 0.36
CMF2	4.27×10^{-5}	71.17	3194.58	-02.73	4.53×10^{-6}	71.55	3920.25	-5.29	6.00	3.42×10^{-6}	71.70	4244.78	-6.59
	0.99989	± 0.00	± 13.66	± 0.40	0.99994	± 0.01	± 27.15	± 0.10		0.99988	± 0.03	± 81.32	± 0.32
At 10 K													
CF	0.00077	89.73	9010.31	-9.94	4.13×10^{-5}	90.76	10466.56	-15.06	11.1	3.66×10^{-5}	90.68	10347.97	-14.59
	0.99979	± 0.03	± 44.54	± 0.13	0.99995	± 0.04	± 60.32	± 0.22		0.99988	± 0.11	± 192.57	± 0.79
CMF1	0.00026	93.56	8534.61	-8.13	3.93×10^{-5}	93.83	8886.13	-09.23	10.1	3.63×10^{-5}	93.54	8425.98	-07.35
	0.99994	± 0.02	± 25.00	± 0.75	0.99996	± 0.03	± 58.91	± 0.22		0.99989	± 0.12	± 195.21	± 0.80
CMF2	0.00012	81.36	8317.21	-05.69	2.14×10^{-5}	81.55	8605.12	-06.64	7.43	1.60×10^{-5}	81.33	8198.05	-04.95
	0.99997	± 0.01	± 19.36	± 0.58	0.99997	± 0.02	± 50.58	± 1.94		0.99994	± 0.08	± 148.81	± 6.14

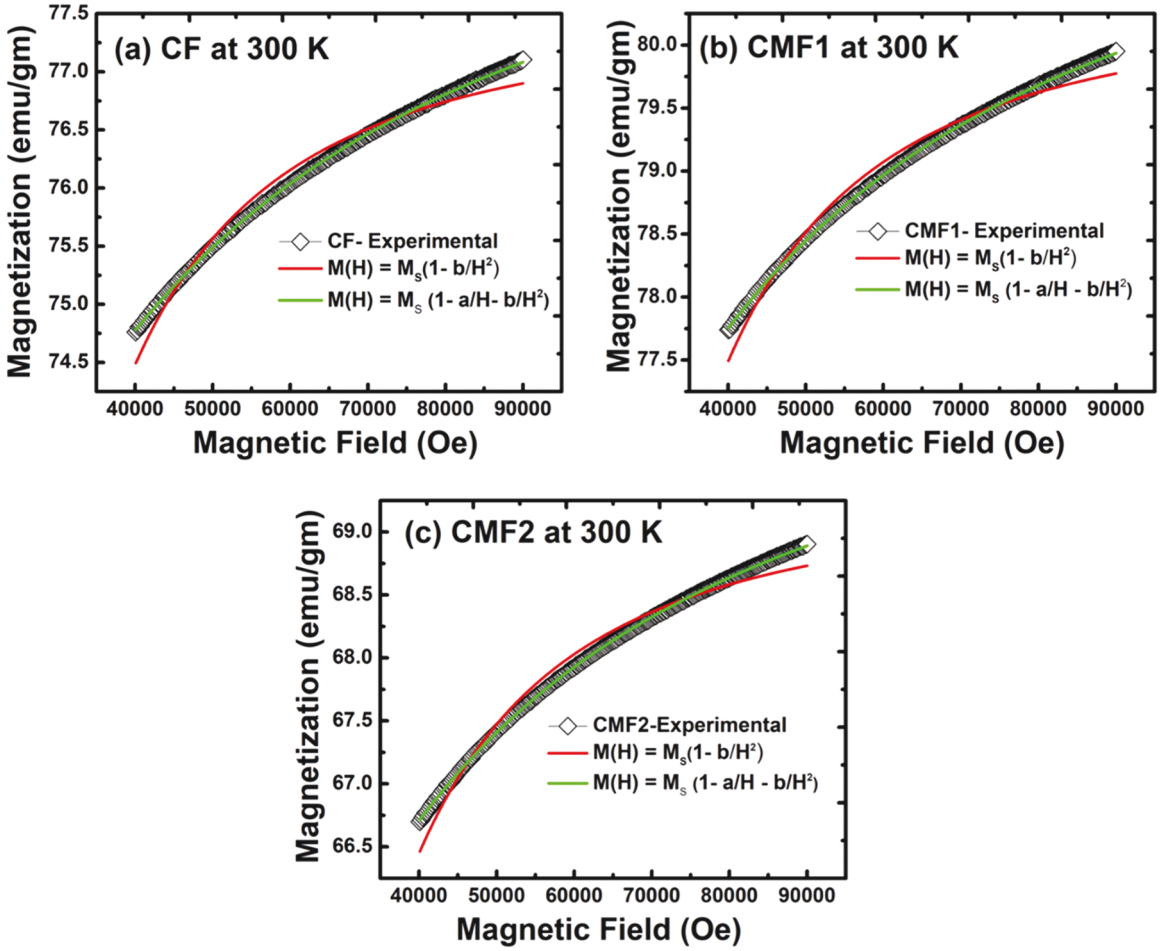

Fig. 9. Fitting to the law of approach using $M(H) = M_S\left(1 - \frac{a}{H} - \frac{b}{H^2}\right)$ and $M(H) = M_S\left(1 - \frac{b}{H^2}\right)$ at field regions 40 < H< 90 kOe for CF (a), CMF1 (b), and CMF2 (c) microgranules at 300 K.

synthesis of Mn-substituted $CoFe_2O_4$ microgranules on a large-scale, which has the potential to be adopted industrially. All the CF and CFM granules created were found to be perfectly spherical and isolated. The SEM and SAXS studies addressed the critical issue and commonly seen scientific challenge of size-distribution of microgranules and the characteristics of individual nano-entities. A better understanding of the factors contributing to the morphology development enables to process control to produce CFM microgranules with controlled morphology. Results from SAXS indicate that the nanostructured microgranules interact with one another in a way that is remarkably identical to that of

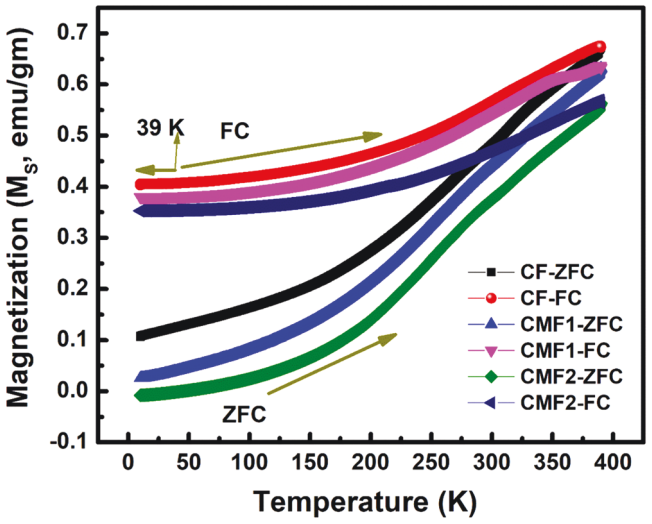

Fig. 10. ZFCFC curves for $Co_{1-x}Mn_xFe_2O_4$ microgranules recorded from 10 to 390 K under an applied field of 100 Oe.

hard spheres. Rietveld's reanalysis of XRD data validates, for all CF and CFM compositions, a single-phase cubic mixed inverse spinel structure. As a result of Mn substitution at the octahedral sites, it is concluded that Co ions are involved in the distortions. By analyzing the Raman spectra, we can see that the Mn substitution of $CoFe_2O_4$ increases the degree of inversion in the cubic inverse spinel structure. The tetrahedral and octahedral positions are occupied by different numbers of divalent (Co^{2+}, Mn^{2+}) and trivalent (Fe^{3+}, Mn^{3+}) cations. Saturation magnetization is enhanced with $x = 0.1$ Mn concentration at 300 K (79.87 emu/gm) and 10 K (86.18 emu/gm). The $Co_{1-x}Mn_xFe_2O_4$ microgranules have a superparamagnetic property above 390 K, as shown by ZFC and FC experiments recorded at 100 Oe field. Our results show that spray drying may be used to produce magnetic microgranules with better magnetic behavior, including the ability to manipulate their size and shape in addition to zero-carbon emissions. We believe that, a more detailed account of necessary fundamental scientific explanation derived from the trends in the local structural parameters and magnetic properties of CF and CMF nanomaterials as presented in this paper may be quite useful for the proposed production method/design to serve as a crucial building block for a wide range of technological applications and be applicable to a large class of spinel ferrites for large scale production with low cost and in a ecofriendly manner.

CRediT authorship contribution statement

YDK conceived and supervised the research. **YDK** and **CVR** managed the funding and project execution. **SMA** synthesized samples and conducted experiments under the close supervision of **YDK. SMA** conducted extensive structural and magnetic measurements. **KH** and **CVR** assisted with data interpretations and literature review analysis. **DS** provided small angle X-ray characterization experiments, analyses, and interpretations. **SMA** and **YDK** coordinated the project and scientific contributions from all the authors. All authors were involved in data analyses, designed figures, and wrote the manuscript while first author (**SMA**) primarily involved in everything. **SMA**, **YDK** and **CVR** coordinated to collect the comments and feedback from all co-authors. Finally, all the authors approved the submission.

Declaration of Competing Interest

The authors declare that they have no known competing financial interests or personal relationships that could have appeared to influence the work reported in this paper.

Data Availability

Data will be made available on request.

Acknowledgments

Bhabha Atomic Research Centre (BARC), India, Grant code: GOI-E-175 supports this research. S. M. would like to thank Dr. Bhavesh B. Sinha of the Center for Nanoscience and Nanotechnology, University of Mumbai, India, for help with magnetic measurements. The authors at the University of Texas at El Paso acknowledge, with pleasure, support from the National Science Foundation (NSF) with NSF-PREM grant #DMR-1827745.

Supporting information

Additional details of CF and CFM samples' EDS data, and composition estimation of all the respective elements/phase, bond angle and bond length extracted from Rietveld refinement of the experimental x-ray diffraction data, and magnetic data at various temperatures with magnetic parameters and fitting to law of approach are included in the supporting information.

Appendix A. Supporting information

Supplementary data associated with this article can be found in the online version at doi:10.1016/j.colsurfa.2023.131697.

References

[1] M. Colombo, S. Carregal-Romero, M.F. Casula, L. Gutiérrez, M.P. Morales, I. B. Böhm, J.T. Heverhagen, D. Prosperi, W.J. Parak, Biological applications of magnetic nanoparticles, Chem. Soc. Rev. 41 (2012) 4306–4334.
[2] D. Zhang, C. Zhou, Z. Sun, L.-Z. Wu, C.-H. Tung, T. Zhang, Magnetically recyclable nanocatalysts (MRNCs): a versatile integration of high catalytic activity and facile recovery, Nanoscale 4 (2012) 6244–6255.
[3] A. Kulandaivel, H. Jawaharlal, Extensive analysis on the thermoelectric properties of aqueous Zn-Doped nickel ferrite nanofluids for magnetically tuned thermoelectric applications, ACS Appl. Mater. Interfaces 14 (2022) 26833–26845.
[4] S.P. Kharat, S.K. Gaikwad, R.C. Kambale, Y.D. Kolekar, C.V. Ramana, Correlation between cation distribution and magnetic and dielectric properties of Dy^{3+}-Substituted Fe-Rich cobalt ferrite, Inorg. Chem. 61 (2022) 19319–19332.
[5] S.M. Ansari, B.B. Sinha, D. Phase, D. Sen, P.U. Sastry, Y.D. Kolekar, C.V. Ramana, Particle size, morphology, and chemical composition controlled $CoFe_2O_4$ nanoparticles with tunable magnetic properties via oleic acid based solvothermal synthesis for application in electronic devices, ACS Appl. Nano Mater. 2 (2019) 1828–1843.
[6] S.E. Shirsath, X. Liu, M.H.N. Assadi, A. Younis, Y. Yasukawa, S.K. Karan, J. Zhang, J. Kim, D. Wang, A. Morisako, Y. Yamauchi, S. Li, Au quantum dots engineered room temperature crystallization and magnetic anisotropy in $CoFe_2O_4$ thin films, Nanoscale Horiz. 4 (2019) 434–444.
[7] S.E. Shirsath, D. Wang, J. Zhang, A. Morisako, S. Li, X. Liu, Single-Crystal-like textured growth of $CoFe_2O_4$ thin film on an amorphous substrate: a self-bilayer approach, ACS Appl. Electron. Mater. 2 (2020) 3650–3657.
[8] S.E. Shirsath, X. Liu, Y. Yasukawa, S. Li, A. Morisako, Switching of magnetic easy-axis using crystal orientation for large perpendicular coercivity in $CoFe_2O_4$ thin film, Sci. Rep. 6 (2016) 30074.
[9] M.A. Almessiere, Y. Slimani, İ.A. Auwal, S.E. Shirsath, A. Manikandan, A. Baykal, B. Özçelik, İ. Ercan, S.V. Trukhanov, D.A. Vinnik, A.V. Trukhanov, Impact of Tm^{3+} and Tb^{3+} rare earth cations substitution on the structure and magnetic parameters of Co-Ni nanospinel ferrite, Nanomaterials 10 (2020) 2384.
[10] V.S. Puli, S. Adireddy, C.V. Ramana, Chemical bonding and magnetic properties of gadolinium (Gd) substituted cobalt ferrite, J. Alloy. Compd. 644 (2015) 470–475.
[11] H.-J. Liu, C.-K. Wang, D. Su, T. Amrillah, Y.-H. Hsieh, K.-H. Wu, Y.-C. Chen, J.-Y. Juang, L.M. Eng, S.-U. Jen, Y.-H. Chu, Flexible heteroepitaxy of $CoFe_2O_4$/Muscovite bimorph with large magnetostriction, ACS Appl. Mater. Interfaces 9 (2017) 7297–7304.
[12] S.G. Kakade, R.C. Kambale, Y.D. Kolekar, C.V. Ramana, Dielectric, electrical transport and magnetic properties of Er^{3+} substituted nanocrystalline cobalt ferrite, J. Phys. Chem. Solids 98 (2016) 20–27.
[13] I. Ali, New generation adsorbents for water treatment, Chem. Rev. 112 (2012) 5073–5091.
[14] W. Wang, S. Gumfekar, Q. Jiao, B. Zhao, Ferrite-grafted polyaniline nanofibers as electromagnetic shielding materials, J. Mater. Chem. 1 (2013) 2851–2859.
[15] C. Fernandes, C. Pereira, M.P. Fernández-García, A.M. Pereira, A. Guedes, R. Fernández-Pacheco, A. Ibarra, M.R. Ibarra, J.P. Araújo, C. Freire, Tailored

design of $Co_xMn_{1-x}Fe_2O_4$ nanoferrites: a new route for dual control of size and magnetic properties, J. Mater. Chem. C. 2 (2014) 5818–5828.
[16] Z. Karimi, L. Karimi, H. Shokrollahi, Nano-magnetic particles used in biomedicine: core and coating materials, Mater. Sci. Eng. C. Mater. Biol. Appl. 33 (2013) 2465–2475.
[17] A.I. Alharthi, E. Abdel-Fattah, J.S.J. Hargreaves, M.A. Alotaibi, I.U. Din, M.N. Al-Shalwi, Influence of Zn and Ni dopants on the physicochemical and activity patterns of $CoFe_2O_4$ derived catalysts for hydrogen production by catalytic cracking of methane, J. Alloy. Compd. 938 (2023), 168437.
[18] S.M. Ansari, R.D. Bhor, K.R. Pai, S. Mazumder, D. Sen, Y.D. Kolekar, C.V. Ramana, Size and chemistry controlled cobalt-ferrite nanoparticles and their anti-proliferative effect against the MCF-7 breast cancer cells, ACS Biomater. Sci. Eng. 2 (2016) 2139–2152.
[19] K.K. Bharathi, R.J. Tackett, C.E. Botez, C.V. Ramana, Coexistence of spin glass behavior and long-range ferrimagnetic ordering in La- and Dy-doped Co ferrite, J. Appl. Phys. 109 (2011) 07A510.
[20] S. Singh, S. Singhal, Transition metal doped cobalt ferrite nanoparticles: Efficient photocatalyst for photodegradation of textile dye, Mater. Today.: Proc. 14 (2019) 453–460.
[21] H. Ghorbani, M. Eshraghi, A.A. Sabouri Dodaran, P. Kameli, S. Protasowicki, C. Johnson, D. Vashaee, Effect of Yb doping on the structural and magnetic properties of cobalt ferrite nanoparticles, Mater. Res. Bull. 147 (2022), 111642.
[22] K. Krieble, M. Devlin, S.J. Lee, S.T. Aldini, J.E. Snyder, Investigation of Ga substitution in cobalt ferrite ($CoGa_xFe_{2-x}O_4$) using Mossbauer spectroscopy, J. Appl. Phys. 103 (2008) 07E508.
[23] Z.M. Abdulhamid, A.A. Sattar, A.S. Darwish, A.A. Ghani, Impact of nanorod morphology on microstructure, magnetic and electrical properties of $Ni_xCo_{1-x}Fe_2O_4$, Phys. B: Condens 601 (2021), 412585.
[24] D.D. Andhare, S.R. Patade, J.S. Kounsalye, K.M. Jadhav, Effect of Zn doping on structural, magnetic and optical properties of cobalt ferrite nanoparticles synthesized via. Co-precipitation method, Phys. B: Condens 583 (2020), 412051.
[25] P. Vlazan, M. Poienar, F.S. Rus, P. Sfirloaga, Study of the structural and magnetic properties of Pd-substituted $CoFe_2O_4$ materials obtained by a fast method, Phys. B: Condens 615 (2021), 413073.
[26] R. Vemuri, G. Raju, M. Gnana Kiran, M.S.N.A. Prasad, E. Rajesh, G. Pavan Kumar, N. Murali, Effect on structural and magnetic properties of Mg^{2+} substituted cobalt nano ferrite, Results Phys. 12 (2019) 947–952.
[27] A. Samavati, A.F. Ismail, Antibacterial properties of copper-substituted cobalt ferrite nanoparticles synthesized by co-precipitation method, Particuology 30 (2017) 158–163.
[28] Y.K. Penke, G. Anantharaman, J. Ramkumar, K.K. Kar, Aluminum substituted cobalt ferrite (Co−Al−Fe) nano adsorbent for arsenic adsorption in aqueous systems and detailed redox behavior study with XPS, ACS Appl. Mater. Interfaces 9 (2017) 11587–11598.
[29] E. Ateia, M. Farag, Synthesis of cobalt/calcium nanoferrites with controllable physical properties, Appl. Phys. A 125 (2019).
[30] S.M. Ansari, K.C. Ghosh, R.S. Devan, D. Sen, P.U. Sastry, Y.D. Kolekar, C. V. Ramana, Eco-Friendly synthesis, crystal chemistry, and magnetic properties of manganese-substituted $CoFe_2O_4$ nanoparticles, ACS Omega 5 (2020) 19315–19330.
[31] A. Manikandan, M. Durka, S.A. Antony, Role of Mn^{2+} doping on structural, morphological, and opto-magnetic properties of spinel $Mn_xCo_{1-x}Fe_2O_4$ ($x = 0.0$, 0.1, 0.2, 0.3, 0.4, and 0.5) nanocatalysts, J. Supercond. Nov. Magn. 28 (2015) 2047–2058.
[32] R.C. Kambale, P.A. Shaikh, N.S. Harale, V.A. Bilur, Y.D. Kolekar, C.H. Bhosale, K. Y. Rajpure, Structural and magnetic properties of $Co_{1-x}Mn_xFe_2O_4$ ($0 \le x \le 0.4$) spinel ferrites synthesized by combustion route, J. Alloy. Compd. 490 (2010) 568–571.
[33] A.B. Salunkhe, V.M. Khot, M.R. Phadatare, N.D. Thorat, R.S. Joshi, H.M. Yadav, S. H. Pawar, Low temperature combustion synthesis and magnetostructural properties of Co–Mn nanoferrites, J. Magn. Magn. Mater. 352 (2014) 91–98.
[34] R. Dou, H. Cheng, J. Ma, S. Komarneni, Manganese doped magnetic cobalt ferrite nanoparticles for dye degradation via a novel heterogeneous chemical catalysis, Mater. Chem. Phys. 240 (2020), 122181.
[35] H. Erdemi, A. Demir, A. Baykal, Electrical properties of triethylene glycol stabilized $Mn_xCo_{1-x}Fe_2O_4$ Nanoparticles, J. Inorg. Organomet. Polym. Mater. 23 (2013) 690–702.
[36] M. Atif, R. Sato Turtelli, R. Grössinger, M. Siddique, M. Nadeem, Effect of Mn substitution on the cation distribution and temperature dependence of magnetic anisotropy constant in $Co_{1-x}Mn_xFe_2O_4$ ($0.0 \le x \le 0.4$) ferrites, Ceram. Int. 40 (2014) 471–478.
[37] B. Guo, Y. Feng, F. Hu, Have carbon emission trading pilot policy improved urban innovation capacity? Evidence from a quasi-natural experiment in China, Environ. Sci. Pollut. Res. (2023), https://doi.org/10.1007/s11356-023-25699-x.
[38] F. Hu, L. Qiu, Y. Xiang, S. Wei, H. Sun, H. Hu, X. Weng, L. Mao, M. Zeng, Spatial network and driving factors of low-carbon patent applications in China from a public health perspective, Front. Public Health 11 (2023) 1–16, https://doi.org/10.3389/fpubh.2023.1121860.
[39] M. Li, Q. Xia, S. Lv, J. Tong, Z. Wang, Q. Nie, J. Yang, Enhanced CO_2 capture for photosynthetic lycopene production in engineered Rhodopseudomonas palustris, a purple nonsulfur bacterium, Green. Chem. 24 (2022) 7500–7518, https://doi.org/10.1039/D2GC02467E.
[40] Y. He, L. Zhang, M.S. Tong, Microwave Imaging of 3D dielectric-magnetic penetrable objects based on integral equation method, IEEE Trans. Antennas Propag. (2023), https://doi.org/10.1109/TAP.2023.3262299.
[41] X. Li, P. Yu, X. Niu, H. Yamaguchi, D. Li, Non-contact manipulation of nonmagnetic materials by using a uniform magnetic field: Experiment and simulation, J. Magn. Magn. Mater. 497 (2020), 165957, https://doi.org/10.1016/j.jmmm.2019.165957.
[42] D. Sen, A. Khan, J. Bahadur, S. Mazumder, B.K. Sapra, Use of small-angle neutron scattering to investigate modifications of internal structure in self-assembled grains of nanoparticles synthesized by spray drying, J. Colloid Interface Sci. 347 (2010) 25–30.
[43] D. Sen, S. Mazumder, J.S. Melo, A. Khan, S. Bhattyacharya, S.F. D'Souza, Evaporation driven self-assembly of a colloidal dispersion during spray drying: volume fraction dependent morphological transition, Langmuir 25 (2009) 6690–6695.
[44] J.S. Pedersen, Determination of size distribution from small-angle scattering data for systems with effective hard-sphere interactions, J. Appl. Crystallogr. 27 (1994) 595–608.
[45] Small angle x-ray scattering / edited by O. Glatter and O. Kratky, Academic Press, London; New York, 1982.
[46] L.G. Telser, The Lognormal Distribution, in: J. Aitchison, J.A.C. Brown (Eds.), Am. J. Agric. Econ., 41, Cambridge University Press, Cambridge, England, 1959, pp. 161–162, 1957, Pp. xviii, 176. $6.50.
[47] S.V.G. Menon, C. Manohar, K.S. Rao, A new interpretation of the sticky hard sphere model, Chem. Phys. Lett. 95 (1991) 9186–9190.
[48] D. Sen, A. Das, J. Bahadur, N. Choudhury, Dynamic modulation of inter-particle correlation during colloidal assembly in a confined medium: revealed by real time SAXS, Phys. Chem. Chem. Phys. 20 (2018) 13271–13278.
[49] Y.D. Kolekar, L.J. Sanchez, C.V. Ramana, Dielectric relaxations and alternating current conductivity in manganese substituted cobalt ferrite, J. Appl. Phys. 115 (2014), 144106.
[50] S.M. Ansari, B.B. Sinha, D. Sen, P.U. Sastry, Y.D. Kolekar, C.V. Ramana, Effect of oleylamine on the surface chemistry, morphology, electronic structure, and magnetic properties of cobalt ferrite nanoparticles, Nanomaterials 12 (2022) 3015.
[51] K.J. Standley (by), in: K.J. Standley (Ed.), Oxide magnetic materials, Clarendon Press, Oxford, 1972.
[52] M.A. Islam, A.K.M.A. Hossain, M.Z. Ahsan, M.A.A. Bally, M.S. Ullah, S.M. Hoque, F. A. Khan, Structural characteristics, cation distribution, and elastic properties of Cr^{3+} substituted stoichiometric and non-stoichiometric cobalt ferrites, RSC Adv. 12 (2022) 8502–8519.
[53] D.E. Sands, Introduction to crystallography, Cour. Corp. (1993).
[54] C.V. Ramana, B.S. Naidu, O.M. Hussain, R. Pinto, Low-temperature growth of vanadium pentoxide thin films produced by pulsed laser ablation, J. Phys. D: Appl. Phys 34 (2001) 35–39.
[55] S.M. Ansari, S.R. Suryawanshi, M.A. More, D. Sen, Y.D. Kolekar, C.V. Ramana, Field emission properties of nano-structured cobalt ferrite ($CoFe_2O_4$) synthesized by low-temperature chemical method, Chem. Phys. Lett. 701 (2018) 151–156.
[56] S.M. Ansari, V. Kashid, H. Salunke, D. Sen, Y.D. Kolekar, C.V. Ramana, First-principles calculations of the electronic structure and magnetism of nanostructured $CoFe_2O_4$ microgranules and nanoparticles, Phys. Rev. B 102 (2020), 035446.
[57] A. Yang, C.N. Chinnasamy, J.M. Greneche, Y. Chen, S.D. Yoon, Z. Chen, K. Hsu, Z. Cai, K. Ziemer, C. Vittoria, V.G. Harris, Enhanced Néel temperature in Mn ferrite nanoparticles linked to growth-rate-induced cation inversion, Nanotechnology 20 (2009), 185704.
[58] S. Sun, H. Zeng, D.B. Robinson, S. Raoux, P.M. Rice, S.X. Wang, G. Li, Monodisperse MFe_2O_4 (M = Fe, Co, Mn) Nanoparticles, J. Am. Chem. Soc. 126 (2004) 273–279.
[59] T. Bala, C.R. Sankar, M. Baidakova, V. Osipov, T. Enoki, P.A. Joy, B.L. Prasad, M. Sastry, Cobalt and magnesium ferrite nanoparticles: preparation using liquid foams as templates and their magnetic characteristics, Langmuir 21 (2005) 10638–10643.
[60] A.L. Tiano, G.C. Papaefthymiou, C.S. Lewis, J. Han, C. Zhang, Q. Li, C. Shi, A.M. M. Abeykoon, S.J.L. Billinge, E. Stach, J. Thomas, K. Guerrero, P. Munayco, J. Munayco, R.B. Scorzelli, P. Burnham, A.J. Viescas, S.S. Wong, Correlating size and composition-dependent effects with magnetic, mössbauer, and pair distribution function measurements in a family of catalytically active ferrite nanoparticles, Chem. Mater. 27 (2015) 3572–3592.
[61] M.F. Hansen, S. Mørup, Estimation of blocking temperatures from ZFC/FC curves, J. Magn. Magn. Mater. 203 (1999) 214–216.
[62] S. Bhattacharyya, J.-P. Salvetat, R. Fleurier, A. Husmann, T. Cacciaguerra, M.-L. Saboungi, One step synthesis of highly crystalline and high coercive cobalt-ferrite nanocrystals, Chem. Commun. (2005) 4818–4820.
[63] B.D. Cullity, S.R. Stock, Elements of X-ray Diffraction, Pearson, 2014.
[64] S.M. Ansari, B.B. Sinha, K.R. Pai, S.K. Bhat, Y.-R. Ma, D. Sen, Y.D. Kolekar, C. V. Ramana, Controlled surface/interface structure and spin enabled superior properties and biocompatibility of cobalt ferrite nanoparticles, Appl. Surf. Sci. 459 (2018) 788–801.
[65] E.C. Devi, I. Soibam, Law of approach to saturation in Mn–Zn ferrite nanoparticles, J. Supercond. Nov. Magn. 32 (2019) 1293–1298.
[66] S.T. Xu, Y.Q. Ma, G.H. Zheng, Z.X. Dai, Simultaneous effects of surface spins: rarely large coercivity, high remanence magnetization and jumps in the hysteresis loops observed in $CoFe_2O_4$ nanoparticles, Nanoscale 7 (2015) 6520–6526.
[67] D. Peddis, F. Orrù, A. Ardu, C. Cannas, A. Musinu, G. Piccaluga, Interparticle interactions and magnetic anisotropy in cobalt ferrite nanoparticles: influence of molecular coating, Chem. Mater. 24 (2012) 1062–1071.
[68] J.L. Weston, Magnetic and structural characterization of magnetoelastic thin films, Univ. Ala. (2002).
[69] S. Laureti, G. Varvaro, A.M. Testa, D. Fiorani, E. Agostinelli, G. Piccaluga, A. Musinu, A. Ardu, D. Peddis, Magnetic interactions in silica coated nanoporous

assemblies of $CoFe_2O_4$ nanoparticles with cubic magnetic anisotropy, Nanotechnology 21 (2010), 315701.
[70] J.M. Vargas, W.C. Nunes, L.M. Socolovsky, M. Knobel, D. Zanchet, Effect of dipolar interaction observed in iron-based nanoparticles, Phys. Rev. B 72 (2005), 184428.
[71] E.C. Stoner, E. Wohlfarth, A mechanism of magnetic hysteresis in heterogeneous alloys, Philos. Trans. R. Soc London Ser. A, Math. Phys. Sci. 240 (1948) 599–642.